University of Central Lancashire
UCLan

Central Lancashire Online Knowledge (CLoK)

Title	"Access of energetic particles to a magnetic flux rope from external magnetic field lines"
Type	Article
URL	https://clok.uclan.ac.uk/35502/
DOI	##doi##
Date	2020
Citation	Laitinen, Timo Lauri mikael orcid iconORCID: 0000-0002-7719-7783 and Dalla, Silvia orcid iconORCID: 0000-0002-7837-5780 (2020) "Access of energetic particles to a magnetic flux rope from external magnetic field lines". The Astrophysical Journal, 906 (1). ISSN 0004-637X
Creators	Laitinen, Timo Lauri mikael and Dalla, Silvia

It is advisable to refer to the publisher's version if you intend to cite from the work. ##doi##

For information about Research at UCLan please go to http://www.uclan.ac.uk/research/

All outputs in CLoK are protected by Intellectual Property Rights law, including Copyright law. Copyright, IPR and Moral Rights for the works on this site are retained by the individual authors and/or other copyright owners. Terms and conditions for use of this material are defined in the http://clok.uclan.ac.uk/policies/

The Astrophysical Journal, 906:9 (10pp), 2021 January 1 https://doi.org/10.3847/1538-4357/abc622
© 2020. The Author(s). Published by the American Astronomical Society.
OPEN ACCESS

Access of Energetic Particles to a Magnetic Flux Rope from External Magnetic Field Lines

T. Laitinen and S. Dalla
Jeremiah Horrocks Institute, University of Central Lancashire, Preston, UK; tlmlaitinen@uclan.ac.uk
Received 2020 August 14; revised 2020 October 27; accepted 2020 October 28; published 2020 December 29

Abstract

Cosmic-ray (CR) fluxes in the heliosphere are affected by the transient interplanetary coronal mass ejections (ICMEs), causing so-called Forbush decreases (FDs), characterized by a decline of up to 25% in the neutron monitor counts at the Earth's surface, lasting up to over a week. FDs are thought to be caused by the ICME shock wave or the magnetic flux rope embedded in the ICME inhibiting CR propagation through the ICME structure. FDs are typically modeled as enhanced diffusion within the ICME structure. However, so far modeling has not considered the access of the CRs from the interplanetary field lines into the isolated magnetic field lines of the ICME flux rope. We study the effect of an ICME flux rope on particle propagation by using full-orbit particle simulations, with the interface between the external interplanetary magnetic field and the isolated flux rope field lines modeled analytically. We find that the particles can access the flux rope through the x-point region, where the external magnetic fields cancel the azimuthal component of the rope field. The transport through this region is fast compared to diffusive radial propagation within the rope. As a result, the propagation of CRs into the flux rope can be modeled as diffusion into a cylinder. The density cavity within the rope is asymmetric, and limited to the magnetic field lines isolated from the external field. Thus, in order to evaluate the role of the flux rope in FDs, one must analyze the extent of the region where the flux rope magnetic field lines are separated from the interplanetary magnetic fields.

Unified Astronomy Thesaurus concepts: Forbush effect (546); Galactic cosmic rays (567); Solar coronal mass ejections (310); Interplanetary physics (827); Interplanetary magnetic fields (824); Interplanetary turbulence (830)

1. Introduction

Propagation of cosmic rays (CRs) in the heliosphere is controlled by the electromagnetic fields within the solar wind plasma. The mean magnetic field of the plasma has a Parker spiral shape, and it is overlaid with plasma turbulence, which causes stochasticity in the propagation of CRs. The CR propagation is also affected by large-scale stable and transient features in the heliosphere such as corotating interaction regions and interplanetary coronal mass ejections (ICMEs).

The large-scale heliospheric structures are known to cause sudden decreases in the intensities of high-energy galactic cosmic rays (GCRs), which have their sources outside the heliosphere. These Forbush decreases (Forbush 1937; Lockwood 1971; Cane 2000; Richardson & Cane 2011) are usually attributed to ICMEs, although also corotating interaction regions and heliospheric current sheet crosses can affect the GCR intensities (e.g., Richardson et al. 1999; Thomas et al. 2014). The magnitude of GCR intensity decrease varies from event to event, reaching up to 25% as measured by neutron monitors, and has a dependency on particle rigidity R of $R^{-\gamma}$ with γ ranging between 0.4 and 1.2 (e.g., Cane 2000).

The Forbush decreases often show a two-step temporal structure (Barnden 1973; Cane 2000). The slowly evolving component starts with a gradual decay of the CR fluxes lasting for several hours, with subsequent recovery that typically takes several days, up to over a week. This slow component is typically considered to be due to GCRs having to penetrate the ICME-driven shock wave and its turbulent downstream as they arrive from the outer heliosphere to be observed at Earth. Within the slowly evolving Forbush decrease, the CR fluxes can experience additional reduction, lasting typically one day and characterized by a fast decay and fast recovery. This faster component is attributed to the particles experiencing the barrier formed by the isolated magnetic flux rope within the ICME (e.g., Cane 2000).

The contribution of the slow and fast components to the depth of the Forbush decrease varies from event to event, but in general they are comparable in terms of the Forbush decrease effect they produce (e.g., Wibberenz et al. 1998; Richardson & Cane 2011). Thus it is important to be able to characterize the FD effects due to the shock and the flux rope separately through modeling.

The effect of the shock wave on the GCR flux is typically modeled as a propagating diffusive barrier, typically using a 1D steady-state diffusion or cosmic-ray modulation model (e.g., Wibberenz et al. 1998, and references therein). The models use the change of the radial diffusion coefficient, solar wind speed, and the barrier size as parameters for the depth of the decrease, and can produce decreases of 1%–10% for diffusion coefficient increases of a factor of 10 within the barrier. The 2D transport model of Le Roux & Potgieter (1991), incorporating both drift and diffusion within the Parker transport model (Parker 1965), successfully reproduced both the amplitude and temporal profile of observed Forbush decreases, whereas Luo et al. (2017) recently used a 3D Fokker-Planck approach to investigate the effects of a wavy heliospheric current sheet on the temporal profiles of Forbush decreases.

The modeling of the effect of the magnetic cloud on the GCR propagation requires a more involved approach, as the cloud is typically characterized by a flux rope-like magnetic structure, which should be taken into account. In a flux-rope configuration, GCRs must propagate across the magnetic field within the cloud to penetrate closer to the cloud axis. Several studies have used approximations based on GCR modulation models and estimations of diffusive filling of the magnetic cloud to evaluate the maximum depth of the Forbush decrease

This is an open access article distributed under the terms of the Creative Commons Attribution 4.0 License.
Any further distribution of this work must maintain attribution to the author(s) and the title of the work, journal citation and DOI.

due to the flux rope (e.g., Quenby et al. 2008; Subramanian et al. 2009), successfully reproduced Forbush decreases in specific case studies by adjusting the diffusion coefficient magnitude. A time-dependent diffusion approach was first used in 1D by Cane et al. (1995) who modeled an observed FD with radial diffusion coefficient $\kappa_{\rm radial} \sim 10^{19}\,{\rm cm^2\,s^{-1}}$. The approach has been recently refined by other authors, for example, Munakata et al. (2006) studied the expansion of the flux rope and the resulting adiabatic deceleration, and Dumbović et al. (2018) investigated different flux rope expansion models. The parameter fits for specific events analyzed in these studies vary significantly, between $\kappa_{\rm radial} \sim 10^{19}$–$10^{21}\,{\rm cm^2\,s^{-1}}$.

Also nondiffusive propagation of particles guided by the flux rope magnetic fields has been addressed recently. Krittinatham & Ruffolo (2009) investigated the role of guiding center drifts in transporting CRs into a flux rope. They followed the GCR guiding center orbits within the 3D toroidal flux rope starting from the edge of the toroid, and found that drifts could trap GCRs on closed orbits for long time periods. However, to keep the CRs within the rope, and for them to propagate deeper into the rope, another cross-field propagation mechanism is needed. Similar results were found by Kubo & Shimazu (2010), who used analytical and numerical solutions of 3D equations of CR motion inside a flux rope. Benella et al. (2019) simulated particles with the 3D equation of motion, without scattering or diffusion, in a magnetic field of an observed flux rope reconstructed using the Grad–Shafranov method. In their case study they were able to reconstruct the observed FD caused by a small flux rope of 6 hr in duration and 0.04 au in reconstructed diameter.

However, the above studies only model the GCR propagation within the flux rope, with the particles injected from the flux rope surface. Such models assume that the access of the CRs from the open interplanetary field lines to the isolated field lines of the flux rope is not hindered by the possibly singular magnetic connection between the external and the rope magnetic field lines. In this work, we investigate the validity of this assumption by studying the particle penetration into a flux rope from ambient constant background magnetic field. We make use of a model that includes an analytic description of the interface between the background magnetic field and the isolated field lines of the flux rope. We numerically solve the fully 3D equations of motion for the test particles and incorporate scattering in velocity space. The full-orbit simulations naturally include the drifts the particles experience within the magnetic field structure. In addition, the particles propagate across the magnetic field due to the random-walk of the particles' gyrocenters when the particle velocities are isotropized. We compare the 3D simulations with a simple radial diffusion model describing diffusion of particles into a cylinder. The models are introduced in Section 2, with further details of the diffusion model in the Appendix. The results are presented in Section 3, with a discussion in Section 4, and conclusions are gathered in Section 5.

2. Models

2.1. Flux Rope Model

We model the flux rope magnetic field using the force-free description by Gold & Hoyle (1960), where, in cylindrical coordinates (r, ϕ, Z), the magnetic field is given by

$$\boldsymbol{B}_{\rm GH} = \frac{B_a\, b\, r}{b^2 r^2 + 1}\,\hat{\boldsymbol{e}}_\phi + \frac{B_a}{b^2 r^2 + 1}\,\hat{\boldsymbol{e}}_Z, \tag{1}$$

where B_a is the axial field, and b is a parameter describing the number of windings around the axis, per unit length of the flux rope along the Z-axis. The field of the flux rope is generated by a field-aligned current, consistently with the Ampere's law, $\nabla \times \boldsymbol{B}_{\rm GH} = \mu_0 \boldsymbol{J}_{\rm GH}$, giving

$$\boldsymbol{J}_{\rm GH} = \frac{1}{\mu_0}\frac{2\,b}{1 + b^2 r^2}\,\boldsymbol{B}_{\rm GH}. \tag{2}$$

The current system generating the Gold-Hoyle field is not limited in r, which is not feasible in reality. In observations of interplanetary magnetic clouds, the extent of the magnetic flux rope is limited (e.g., Burlaga et al. 1981). To achieve such a cutoff of the magnetic field requires a current system in which the axial current that produces the azimuthal magnetic field is counteracted by a current flowing in the opposite direction. To our knowledge there are no observations of such a current system at present. Thus, instead of attempting to limit the flux rope magnetic field by formulating a current system, we opt for limiting the magnetic field directly. For this purpose, we use a modulating function

$$f(s) = 2\,s^3 - 3\,s^2 + 1, \tag{3}$$

which goes from 1 to 0 as the variable s goes from 0 to 1, and has a vanishing derivative at 0 and 1. We use the modulating function to smoothly cut off the magnetic field at rope radius r_b, over a sheath region of thickness t_b, by using

$$\boldsymbol{B}_r = \begin{cases} \boldsymbol{B}_{\rm GH}(r) & r < r_b \\ f\left(\frac{r - r_b}{t_b}\right)\boldsymbol{B}_{\rm GH} & r_b \leqslant r < r_b + t_b \\ 0 & r \geqslant r_b + t_b, \end{cases} \tag{4}$$

which fulfills the condition $\nabla \cdot \boldsymbol{B} = 0$.

The magnetic flux rope is superposed on a background magnetic field. In this work, we consider constant a background magnetic field B_0, thus giving the total magnetic field as

$$\boldsymbol{B} = \boldsymbol{B}_{\rm r} + \boldsymbol{B}_0. \tag{5}$$

We align the flux rope so that in Cartesian coordinates (x, y, z) its axial magnetic field is directed in the positive x direction, and the background magnetic field is aligned in the z direction thus $\boldsymbol{B}_0 = B_0\,\hat{\boldsymbol{e}}_z$, where B_0 is the magnitude of the background field. We use $B_0 = 5$ nT, consistent with the observed interplanetary magnetic field at 1 au from the Sun. In future work, we will also investigate other relative orientations between the rope axis and the background magnetic field.

We show the z-component of the magnetic field used in the simulations in Figure 1(a) for flux rope parameters $B_a = 5B_0$, $b^{-1} = 14\,{\rm r}_\odot$ and $r_b = 32\,{\rm r}_\odot$, where ${\rm r}_\odot$ is the solar radius. The parameters have been selected based on a case study of a flux rope analyzed in Dasso et al. (2006). The solid blue curve shows Gold-Hoyle rope field, as given by Equation (1), and the dashed red and dashed–dotted black lines show the field given by Equation (4) for two boundary thicknesses t_b. As can be seen, the unlimited solution shown by the blue curve displays no boundary for the flux rope extent, whereas using a finite boundary thickness results in finite flux rope.

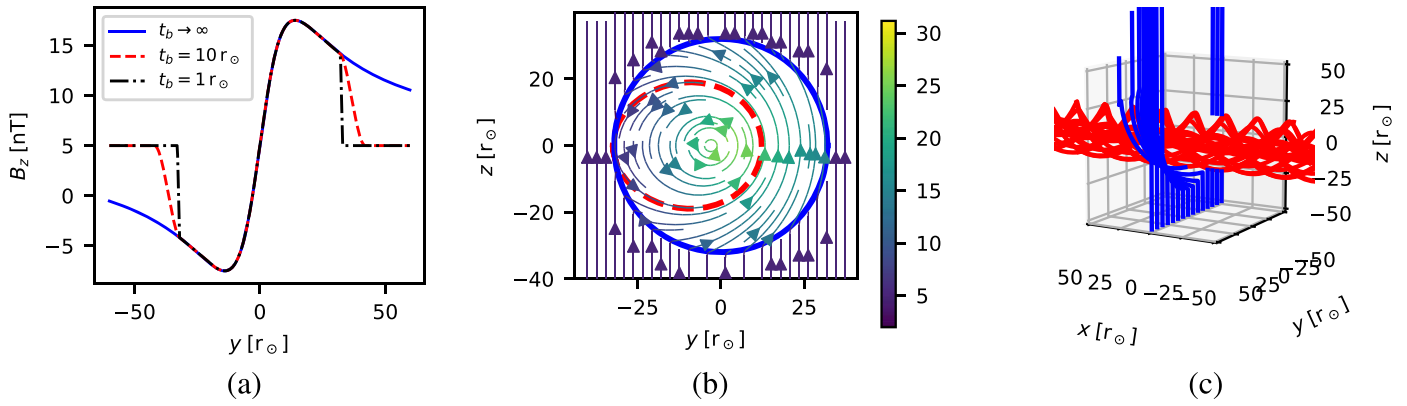

Figure 1. (a) The z-component or the toroidal component, of the magnetic field ($B_z(z = 0)$) through the axis of the flux rope, for configuration where the constant background field is aligned with the z-axis, and the rope axis along the x-axis. The solid blue curve shows the field for an infinite Gold-Hoyle flux rope, while the dashed red and dashed–dotted black curves show the cases where the field is decayed to zero from the radius, $r_b = 32\,r_\odot$ within a boundary layer of thickness $t_b = 10\,r_\odot$ and $t_b = 1\,r_\odot$ respectively. (b) A $y - z$ projection of the magnetic field of the flux rope with $t_b = 1\,r_\odot$. The red curve depicts the boundary between the isolated flux rope field lines and the open background magnetic field. The thick blue circle denotes the extent of the flux rope, as given by r_b. (c) A 3D projection of the magnetic field of the flux rope. The red curves represent the field isolated within the rope, whereas the blue field lines are open.

In Figure 1(b) we show a $y - z$-projection of the rope magnetic field, with the projected magnetic fields shown by the thin color-coded lines. The red curve is the separating boundary, or a surface, between the field lines that are isolated within the flux rope and those connected to the external open field. The thick blue curve shows the extent of the flux rope, as given by parameter r_b. It should be noted that the structure is asymmetric, and the separated field encloses only a fraction of the range defined by the flux boundary radius, r_b. The x-point, where the y and z components of the background and rope fields cancel is located at $(y, z) \approx (-32, 0)r_\odot$.

In addition, in Figure 1(c), we show the 3D structure of the rope and the enclosing field. The red curves trace the field lines within the flux rope, and the blue curves the open field lines outside of the separated flux rope field lines. As can be seen, the external field is disrupted in the direction along the axis of the flux rope (the blue curves on the near side of the red axis field lines), due to the toroidal field.

2.2. Particle Simulations

We analyze the charged particle propagation in a flux rope by use of full-orbit simulations that solve the full 3D Lorentz equation. The simulation method is described in more detail in Dalla & Browning (2005). The particle propagation is investigated as the particles penetrate the flux rope field from below or above the flux rope. For statistical efficiency, we employ the Liouville theorem to trace the particles as phase space elements backward in time, injecting them within the region of interest, and tracing them until they reach an injection surface, or until a predetermined simulation time has lapsed.

We will also employ scattering in the simulations. The scattering is included as pitch- and phase angle isotropization at scattering events parameterized by scattering time $\tau_{sc} = \lambda_{sc}/v$, where λ_{sc} is the parallel scattering mean free path, which for simplicity is kept constant in the simulations, and v is the particle velocity. At a scattering event, the particle's post-scattering velocity vector will be drawn from an isotropic distribution, keeping the magnitude of the velocity constant. The scattering will facilitate decoupling of the particle from the field line it was on before scattering, as the particle's gyrocenter will move a distance of the order of its Larmor radius. Thus, the scattering will cause the particle's gyrocenter to move stochastically across the magnetic field lines.

It should be noted that the stochastic random-walk of the particles across the magnetic field described above is slow compared to the transport of particles across the mean field as they propagate along random-walking field lines in the turbulent plasmas (e.g., Fraschetti & Jokipii 2011). The latter is typically considered to dominate cross-field CR transport, and is the basis of the theories connecting the plasma turbulence properties to the CR cross-field diffusion coefficients used in Fokker-Planck equation-based modeling of CRs (e.g., Jokipii 1966; Matthaeus et al. 2003; Shalchi 2010; Ruffolo et al. 2012; Laitinen & Dalla 2017). However, as shown by Ghilea et al. (2011), in 2D-dominated turbulence the turbulently random walking field lines tend to follow the 2D equipotential contours of the magnetic field. In a flux rope such as the one modeled in this project, the equipotential contours are mainly azimuthal. Thus, as first approximation we assume that the field line random walk does not contribute appreciably to the propagation of CRs radially toward the axis of the flux rope, and do not introduce cross-field transport of CRs due to random-walking field lines in this study.

We show samples of particle traces from our simulations in Figure 2 for $\lambda_{sc} = 0.1$ and 0.3 au for the flux rope shown in Figure 1. The blue circle depicts the flux rope radius r_b, and the red circle the surface separating the open and isolated field lines. The thin helical lines show the orbits of particles of different energies, as given by the legend in both figures. As can be seen in Figure 2(a), the low-energy particles are mainly confined to areas either outside or inside the isolated field lines. However, with sufficient scattering, in this case with $\lambda_{sc} = 0.1$ au, some particles can enter the isolated field lines through the x-point on the left side of the flux rope. Inside the flux rope, the particles quickly fill the toroidal magnetic field lines of the cloud, and can propagate in the radial direction through scattering.

The higher-energy particles, shown in Figure 2 (b), have larger Larmor radii, and thus their access due to the gyrocenter decoupling is more efficient. The particles still mostly enter the isolated field lines at or close to the x-point on the left side of the flux rope, however, through a larger area, and as a result they can penetrate the isolated field lines already with less

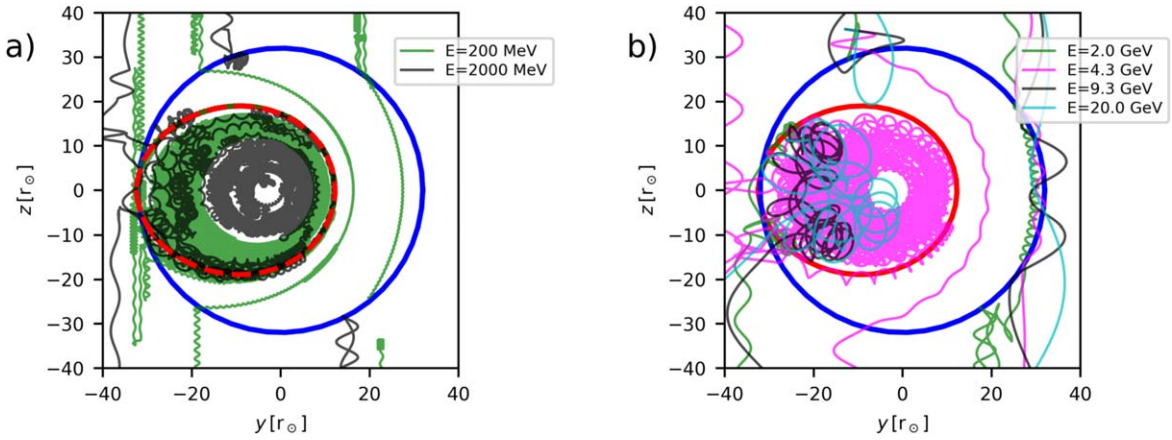

Figure 2. A sample of particles with energies relevant to SEPs propagating in and around the flux rope presented in Figure 1. The blue circle shows the flux rope radius $r_b = 32r_\odot$. The parallel mean free path of the particles is 0.1 and 0.3 au in panels (a) and (b), respectively.

frequent scattering. They are also able to propagate radially within the flux rope more efficiently, as well as to again escape the flux rope.

It should be noted that the ease of access of particles to the isolated field lines is clearly a finite Larmor radius effect: in guiding center approximation, the particles could access the flux rope only through the singular point (or singular line in 3D). Thus, it is necessary to use a fully 3D equation of motion for the particles in order to analyze the particle access to the isolated magnetic structure within a flux rope.

2.3. Diffusion Model

Particle propagation inside a flux rope is often modeled using a diffusion-convection approach, with Fokker-Planck, Parker, or diffusion equation (e.g., Cane et al. 1995; Munakata et al. 2006; Quenby et al. 2008; Subramanian et al. 2009; Dumbović et al. 2018). We compare our test particle modeling results to those obtained via a diffusion approach by using a simple radial diffusion equation for the density of particles, $n(r, t)$, defined as

$$\frac{\partial n(r,t)}{\partial t} = \frac{1}{r}\frac{\partial}{\partial r} r\, \kappa_{\rm radial}(r) \frac{\partial n}{\partial r}. \quad (6)$$

The diffusion coefficient for a random-walk process with step size Δr at intervals τ, at the limit of large time and large number of scatterings is defined as

$$\kappa_{\rm radial} = \frac{(\Delta r)^2}{2\tau}. \quad (7)$$

In our simulations, the randomization of the velocity vector at scattering events results in random-walk of the particle's gyrocenter. Simplifying our analysis to the case where the magnetic field is aligned with the x-axis, a particle at $(y(t), z(t)$ has its gyrocenter (y_G, z_G) initially at

$$y_{G0} = y(t) - r_L\sqrt{1-\mu_0^2}\cos(\Omega t + \phi_0) \quad (8)$$

$$z_{G0} = z(t) - r_L\sqrt{1-\mu_0^2}\sin(\Omega t + \phi_0), \quad (9)$$

where μ_0 and ϕ_0 are the pitch angle cosine and the phase angle at $t = 0$, respectively, $\Omega = qB/\gamma m$ is the gyrofrequency, $r_L = v/\Omega$ is the particle's Larmor radius, and $\gamma = 1/\sqrt{1-(v/c)^2}$ is the Lorentz factor with c being the speed of light.

If the velocity vector is now scattered to give new values μ_1 and ϕ_1, the change in the gyrocenter will be, say, for the y-coordinate,

$$\Delta y_G = r_L\sqrt{1-\mu_0^2}\cos(\Omega t + \phi_0) - r_L\sqrt{1-\mu_1^2}\cos(\Omega t + \phi_1). \quad (10)$$

Averaging the square of the deviation over the velocity space (assumed to be isotropic), we find

$$\langle \Delta y_G^2 \rangle = \frac{2}{3} r_L^2. \quad (11)$$

Thus, a diffusion coefficient that corresponds to our simulations is of the form

$$\kappa_{\rm radial} = \frac{r_L^2}{3\tau_{\rm sc}}. \quad (12)$$

This form of the cross-field diffusion coefficient was given also in, e.g., Parker (1965).

In our full-orbit simulations, the parallel scattering timescale $\tau_{\rm sc}$ is kept constant. However, the Larmor radius of a particle depends on the magnitude of the magnetic field. As a result, the cross-field diffusion coefficient is considerably smaller within the rope, by a factor of $\sim(B_0/B_a)^2$ (see Equations (1) and (5)), and varies as r^{-4} for $1/b \lesssim r \lesssim r_b$.

It should be noted that as we use time-backward integration within the full-orbit model, the cross-field decoupling of the particle from its field line depends on the magnetic field at the location where the scattering event occurs. As a result, the cross-field propagation in our simulations cannot be considered as averaged over a Larmor orbit, which would be more natural for considering decoupling of the particles. We will consider other parameterizations of the scattering and cross-field diffusion in future studies.

Equation (6) is solved using the Crank–Nicolson method, which is explained in detail in the Appendix.

3. Results

In this study, we investigate the dependence of CR penetration into a flux rope on the particle energy and scattering parameters, keeping the flux rope parameters fixed

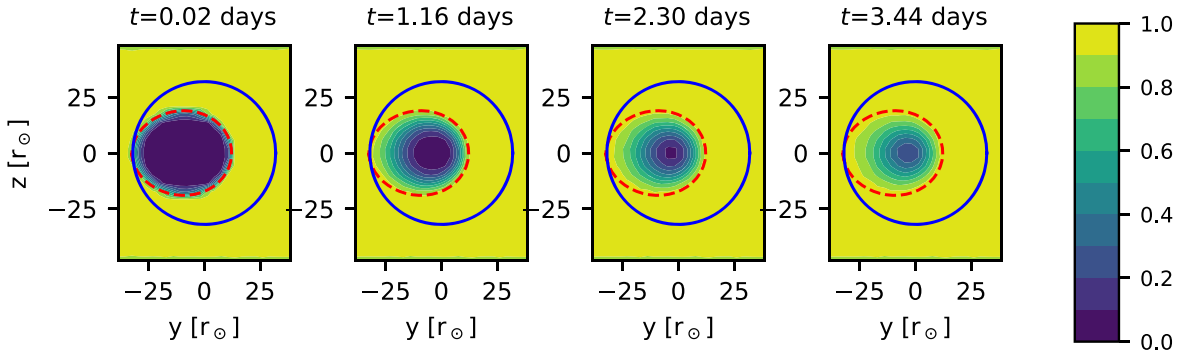

Figure 3. Evolution of 200 MeV proton density inside and in the vicinity of a flux rope, with constant injection of particles above and below the rope. The parallel scattering mean free path is $\lambda_{sc} = 0.1$ au. The dashed curve shows the location of the separator surface between the flux rope and the open field.

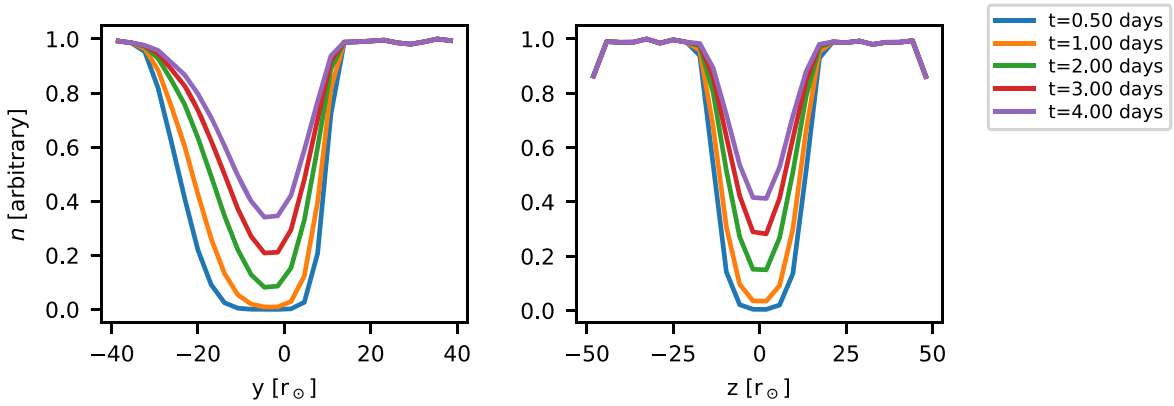

Figure 4. Evolution of 200 MeV proton density profiles through the rope axis along $z = 0$ axis (left) and $y = 0$ axis (right), for the flux rope as shown in Figure 3.

at $B_a = 5B_0$, $b^{-1} = 14\,r_\odot$, $r_b = 32\,r_\odot$, and $t_b = 2\,r_\odot$, and the rope axis normal to the background magnetic field, as shown in Figure 1. In Figure 3, we show an example of the evolution of 200 MeV proton density in the flux rope depicted in Figure 1, as obtained with our test-particle simulations. The parallel mean free path is $\lambda_{sc} = 0.1$ au, representing reasonably strong scattering in the interplanetary space. The particles are injected isotropically at a constant rate at the bottom and top of the box starting from $t = 0$, that is,

$$Q(r, t) = Q_0 \frac{1}{2}(\delta(z - z_0) + \delta(z + z_0))\Theta(t), \qquad (13)$$

where Θ is the Heaviside function. As we are employing a time-backward integration method, the source function $Q(r, t)$ is used as a weighting function. Particles that do not reach either of the injection boundaries within the simulation period receive a weight of 0.

The simulated particles are binned in hourly bins, with the Figure 3 showing the density at selected times. As can be seen, for 200 MeV protons, the evolution of the particle density within the rope is very gradual. This is due to the small gyroradius of the particle, $\sim 0.3\,r_\odot$. Scattering is required for any flux rope penetration for low energies: our simulations (not presented here) show that 200 MeV protons are not able to reach the flux rope axis without scattering.

The area of significant CR depletion is not defined by the flux rope radius (blue circle in Figure 3): the barrier for the particles is formed only by the isolated field region, depicted by the dashed red curve in Figure 3. Once the particles have accessed the flux rope, they quickly isotropize on the toroidal field lines. The particle distribution within the flux rope is asymmetric, due to the asymmetry of the surface separating the flux rope and external magnetic field. At early times (the leftmost contours in Figure 3) the boundary of the particle cavity in the 200 MeV proton density traces the separating surface (red dashed curve). At later times, the contours inside the rope trace the field lines shown in Figure 1(b), with each contour centered progressively closer to the flux rope axis.

In the top panel of Figure 4, we present the one-dimensional density profiles of the 200 MeV protons through the axis of the flux rope, along the y-axis (left panel) and along the z-axis (right panel). As can be seen, the intensity decrease along the y-axis is clearly asymmetric, and the decrease is much wider than the decrease along the z-axis. This is due to the asymmetry in the isolated field region caused by the existence of the external field. The asymmetry is preserved as time progresses and the flux rope is penetrated by more particles.

In Figure 5, we show the proton density profiles 3 days after injection, corresponding to a flux rope propagation time from the Sun to Earth at speed 575 km/s. The top panel shows the effect of particle energy on the propagation of the particles within the flux rope. This can be characterized through the Larmor radius, which for the three energies, 20, 200, and 2000 MeV are $r_L = 0.1$, 0.3, and 1.3 $r_\odot$, respectively (for the ambient background field). For the parallel mean free path of $\lambda_{sc} = 0.1$ au, used in the top panel of Figure 5, the corresponding radial diffusion coefficients can be estimated using Equation (12) as $\kappa_{radial} = 9 \cdot 10^{16}$, $3 \cdot 10^{18}$, and

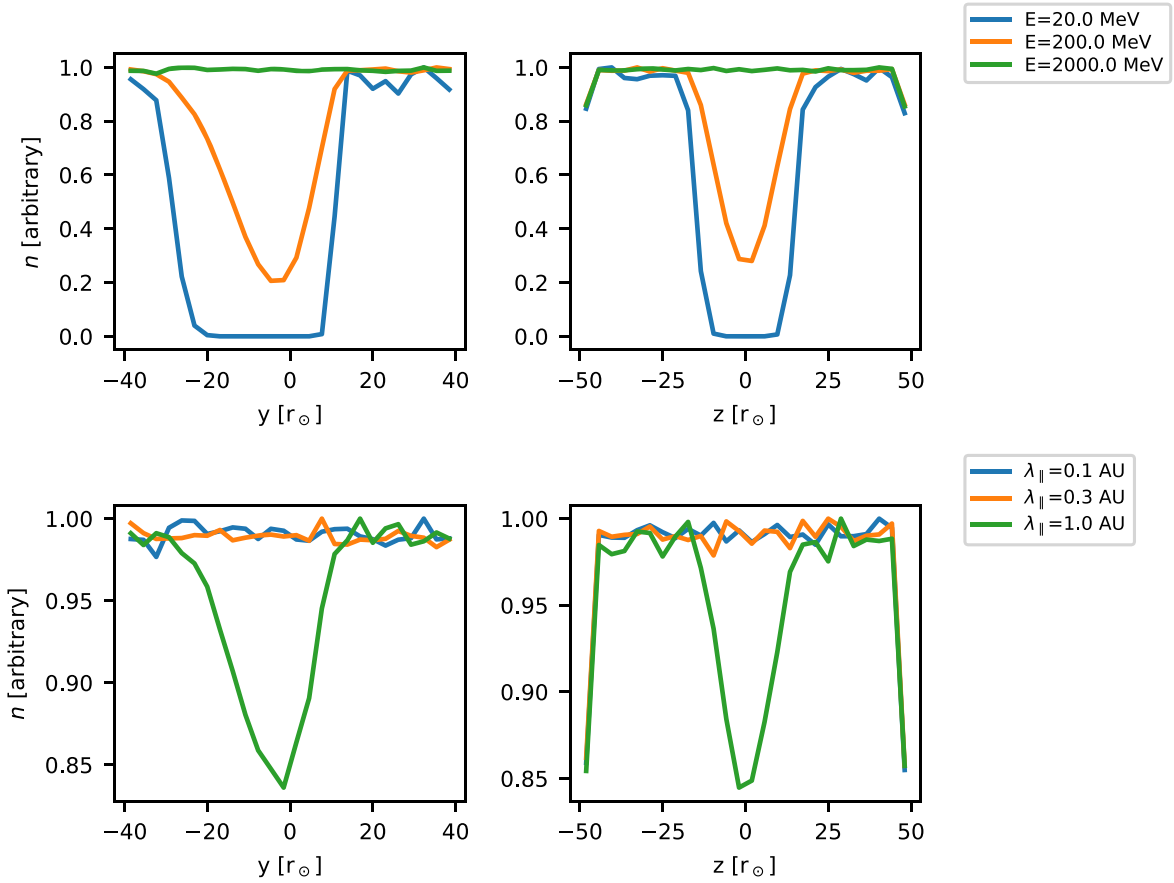

Figure 5. Proton density profiles through the rope axis along $z = 0$ axis (left) and $y = 0$ axis (right), for the flux rope as shown in Figure 3, after 3 days. Top panel: dependence on proton energy, with $\lambda_{sc} = 0.1$ au. Bottom panel: dependence on parallel scattering mean free path, 2 GeV protons.

$9 \cdot 10^{19}\,\mathrm{cm^2\,s^{-1}}$, respectively. Within the flux rope, the diffusion coefficients would be fraction $(B_0/B_a)^2$ of that outside the flux rope, due to the reduction of the Larmor radius in a stronger field. Using these values, we can estimate a cross-field diffusion time of the particles from the rope boundary to the flux rope axis, $\tau_d = r_b^2/(2\kappa_{\mathrm{radial}})$, which for the 2 GeV particle gives 0.33 days in the external field, and 8 days in the axis field. For a 20 MeV proton, the cross-field diffusion time in the ambient field would be over 300 days. Thus, such low-energy protons would not be able to penetrate the flux rope within the propagation time of the flux rope from the Sun to Earth.

In the bottom panel of Figure 5, we show the 2 GeV proton densities 3 days after injection for three different parallel mean free paths, depicting three different turbulent environments within and outside the flux rope. Here, we see the significance of scattering in enabling the particles to penetrate the flux rope: for stronger scattering with $\lambda_{sc} = 0.1$ or 0.3 au the flux rope is fully filled by the 2 GeV protons after 3 days. For $\lambda_{sc} = 1$ au, the radial diffusion coefficient in ambient field can be estimated as $9 \cdot 10^{18}\,\mathrm{cm^2\,s^{-1}}$, with the density profile of similar shape but less deep as for the 200 MeV protons with $\lambda_{sc} = 0.1$ au, as shown in the top panel of Figure 5.

In Figure 6, we show the evolution of 200 MeV protons into a flux rope described in Figure 1 when the propagation is modeled as radial diffusion (see Section 2.3 and the Appendix). As the model is one-dimensional, it can only be used to analyze the radial density profile of particles within the rope. The diameter of the rope is taken to be that of the isolated field line area (red circle in Figure 1(b)) along the y-axis. The diffusion coefficient in Equation (6) is given by Equation (12). In the left panel of Figure 6 we use a constant κ_{radial} within the flux rope, with $r_L = qB_a/m$ in Equation (12). In the right panel we use $r_L = qB_r(r)/m$, resulting in a r^{-4} radial dependence of the diffusion coefficient, as discussed in Section 2.3. This comparison of different radial dependencies of κ_{radial} shows how the radial profile of the CRs depends strongly on whether the diffusion coefficient is consistent with the rope magnetic field, or it is only estimated as constant within the rope.

In Figure 7 we compare the full-orbit simulations (solid curves) and the radial diffusion solution (dashed curves) for different particle energies and parallel mean free paths. The comparison shows that the diffusion equation agrees reasonably well with the full-orbit simulations for a wide range of energy and scattering conditions in the investigated flux rope configuration. The correspondence of the two models implies that the access of the particles into the isolated magnetic field lines inside the flux rope from the external field lines is not significantly hindered by the lack of magnetic connection. As implied by Figure 2, the fast access may be facilitated by the x-point between the isolated and open topologies, where the magnetic tying of the particles to the field lines is at its weakest.

4. Discussion

In this paper, we have used full-orbit test-particle simulations to investigate how high-energy charged particles can enter a magnetic flux rope when they are required to propagate from

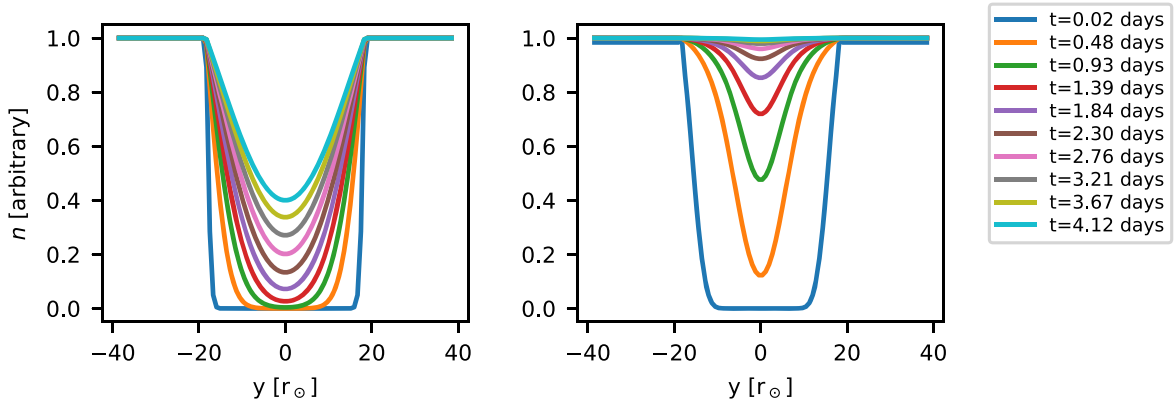

Figure 6. Evolution of 2 GeV proton density profiles through the rope axis, obtained solving the diffusion equation with diffusion coefficient parameterized by $\lambda_{sc} = 1$ au. Left panel: constant diffusion coefficient. Right panel: diffusion coefficient proportional to B^2 within the rope.

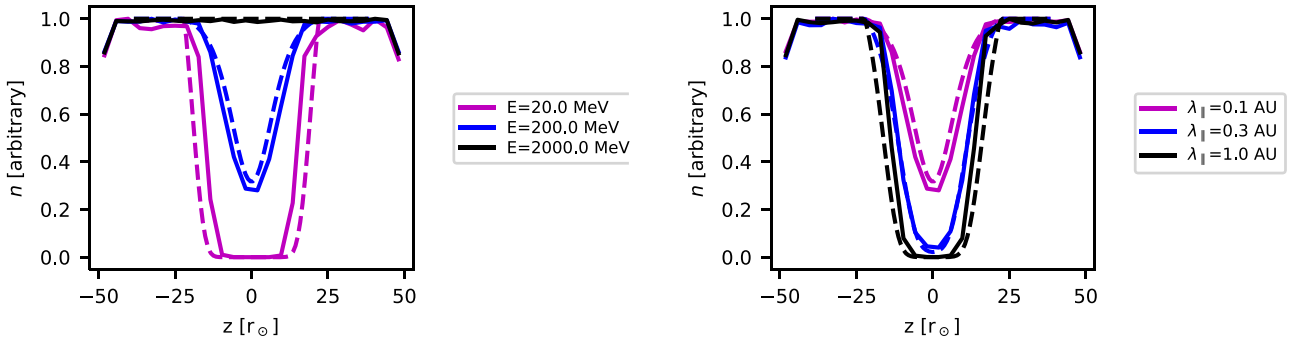

Figure 7. Comparison of the full-orbit simulations (solid curves) and the radial diffusion solution (dashed curves) for the flux rope as shown in Figure 3, after 3 days, with injection rate increasing 1% day^{-1}. Left panel: dependence on proton energy, with $\lambda_{sc} = 0.1$ au. Right panel: dependence on parallel scattering mean free path, for 200 MeV protons.

external, open field lines to the isolated field lines inside the rope. We used a model in which the flux rope is embedded within an undisturbed magnetic field, including a transition from the external field to the flux rope field. We found that the significant size scale for particle propagation is not the scale where the rope magnetic field dominates over the background magnetic field, that is, the rope radius r_b in Equation (4), as the particles within this radius still can be connected to the outside magnetic field (see Figure 1(b)). Only the field lines forming the isolated rope structure constitute a significant barrier to the charged particles. The barrier is asymmetric even for a symmetric rope field, as seen in Figures 3 and 4, since the particles that penetrated into the isolated field lines quickly isotropize along the toroidal field lines, which themselves are asymmetric (Figure 1)(b)).

The question then remains: how fast can the particles access the isolated field lines of the flux rope from the external open field lines? The interface in our model is represented by the x-point, on the left-hand side of the rope in Figure 1(b). Will the singular nature of this contact point hinder the particle access to the isolated field lines?

To analyze this question, we solved a radial diffusion equation with a diffusion coefficient consistent with the full-orbit simulation setup, and compared the diffusion solution with the full-orbit code results. We found that the full-orbit simulation results give similar evolution of particle density within the flux rope as a diffusion model where particles diffuse into the rope from the separator surface. This indicates that the access of the particles into the rope is a fast process as compared to isotropization of particles along the flux rope magnetic fields and the subsequent cross-field diffusion of particles within the flux rope. Our result thus suggests that diffusion-based flux rope simulation methods can be used to model particle propagation into a magnetic flux rope, provided that the radius of the rope is taken as the isolated surface radius instead of the radius where the flux rope is disturbed.

However, this result is dependent on the turbulence conditions of the region around the isolated field region, in particular the turbulence environment around the x-point. With strong turbulence in this region, the particle access to the flux rope may be considerably slower. The superposed epoch study by Masías-Meza et al. (2016) shows that the sheath is more turbulent than the preceding solar wind and the flux rope. However, the parallel and perpendicular particle diffusion coefficients scale as $(B^2_{rms}/B^2)^{\alpha}$ (see Jokipii 1966; Shalchi et al. 2004; Ruffolo et al. 2012; Laitinen et al. 2017, for value of α for different processes), and this quantity does not attain a significant increase in the sheath as compared to the preceding solar wind (Masías-Meza et al. 2016). Thus, the increased turbulence amplitude within the sheath does not necessarily imply significantly larger scattering.

The turbulence conditions within the flux rope can have a significant effect on the filling of the magnetic structure with energetic particles. Our simple scattering model is consistent with a radial diffusion coefficient $\kappa_{radial} = 9 \cdot 10^{18}$ cm^2 s^{-1} for 200 MeV protons and $\lambda_{sc} = 1$ au (Equation (12)), which is close to the Cane et al. (1995) fit of 10^{19} cm^2 s^{-1}. The long parallel mean free path is also consistent with the observed nearly scatter-free parallel propagation conditions within flux

ropes observed in some solar events (e.g., Torsti et al. 2004; Ruffolo et al. 2006; Sáiz et al. 2008; Leske et al. 2012), although the Ruffolo et al. (2006) case study does imply a stronger cross-field diffusion coefficient than ours and that in the case study of Cane et al. (1995). The turbulence within a flux rope has been analyzed by Leamon et al. (1998) who found that the turbulence within an analyzed flux rope was richer in the 2D component of turbulent geometry than undisturbed solar wind, implying a stronger contribution of cross-field diffusion of particles, relative to diffusion along the magnetic field. However, as shown by Masías-Meza et al. (2016), $B_{\rm rms}/B$ is significantly lower within the magnetic cloud, as compared to the sheath region and the undisturbed solar wind. Lower relative turbulence amplitude implies weaker cross-field transport within the cloud, compared to the undisturbed solar wind. In addition, as we discussed earlier, the field lines in 2D-dominated turbulence tend to follow the 2D equipotential contours (Ghilea et al. 2011) and thus may not contribute significantly to transport toward the axis of the flux rope.

Our current study has not addressed the thickness of the boundary layer between the flux rope magnetic field and the background magnetic field, or the flux rope orientation with respect to the background magnetic field. An orientation other than the one in our study, where the rope axis is normal to the external field, will result in expansion of the isolated part of the flux rope if the field strengths are kept the same. This may result in slower filling of the flux rope, and hence deeper and wider CR intensity depressions.We will address these details in a subsequent study. Further, a flux rope is likely to expand as it propagates from the Sun to the interplanetary space, with changing internal magnetic field affecting the diffusion pattern of particles into the flux rope. Such modeling was recently performed in Dumbović et al. (2018), who found qualitative agreement with observed Forbush decreases. We aim to improve our modeling to include an expanding flux rope to account for both the changes in diffusion coefficients, and the resulting adiabatic deceleration of the particles in a future study.

5. Conclusions

In this study we have simulated charged particle access to a magnetic flux rope from external open magnetic field lines. We found that:

1. The decrease of particle density is determined by the size and geometry of the region in which the field lines are completely isolated from the external field.
2. Low-energy particles can penetrate the isolated field lines at or near the x-point between the isolated and open field lines. This is a finite Larmor radius effect, as in guiding center approximation the access could only take place through a singular x-point. High-energy particles can penetrate from a wider area, in the vicinity of the x-point.
3. The spatial distribution of the particle population inside the isolated magnetic field structure is asymmetric, as determined by the magnetic field line structure.
4. Particle access to the isolated fields is rapid compared to the stochastic radial propagation of the particles, and the latter is consistent with a simple radial diffusion model where particles are injected at the isolated magnetic field boundary.

Our findings show that radial diffusion into a cylinder can be a viable model for describing particle penetration into or out of a flux rope. However, care must be taken when describing the extent of the isolated field region, as well as the turbulent region outside it.

T.L. and S.D. acknowledge support from the UK Science and Technology Facilities Council (STFC) (grants ST/M00760X/1 and ST/R000425/1). Access to the University of Central Lancashire's High Performance Computing Facility is gratefully acknowledged.

Appendix
Diffusion Model

The radial diffusion equation

$$\frac{\partial n(r,t)}{\partial t} = \frac{1}{r}\frac{\partial}{\partial r} r\,\kappa_{\rm radial}(r)\frac{\partial n}{\partial r} \tag{A1}$$

can be solved by use of Crank–Nicolson method (e.g., Hutchinson 2015), by discretizing n at locations $r_k = r_0 + k\Delta r$, and times $t^j = t_0 + j\Delta t$. In the derivation below, we will drop the subscript of the diffusion coefficient for clarity.

The outer derivative of the right-hand side of Equation (A1) can be written by evaluating the inner derivative at half-steps, $r_{k\,+\,1/2}$, as

$$M^j = \frac{1}{r_k \Delta r}\left[\kappa'_{k+1/2}\frac{n^j_{k+1}-n^j_k}{\Delta r} - \kappa'_{k-1/2}\frac{n^j_k - n^j_{k-1}}{\Delta r}\right], \tag{A2}$$

where $\kappa' = r\,\kappa$. The matrix can be reorganized to get coefficients for each n^j_k as

$$M^j = \frac{1}{r_k \Delta r^2}[\kappa'_{k+1/2}\,n^j_{k+1} - (\kappa'_{k-1/2} + \kappa'_{k+1/2})\,n^j_k + \kappa'_{k-1/2}\,n^j_{k-1}] \tag{A3}$$

Crank–Nicolson scheme is constructed by evaluating the right-hand side of Equation (A1) at both the previous and new timestep, thus it is a semi-implicit scheme, giving

$$n^{j+1}_k = n^j_k + \frac{\Delta t}{2}M^{j+1} + \frac{\Delta t}{2}M^j \tag{A4}$$

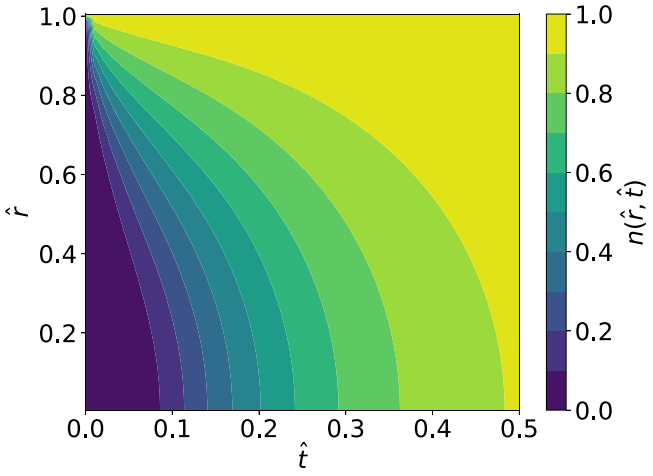

Figure 8. Contour plot of diffusion into cylinder, as a function of normalized time and radius, obtained using the Crank–Nicholson scheme.

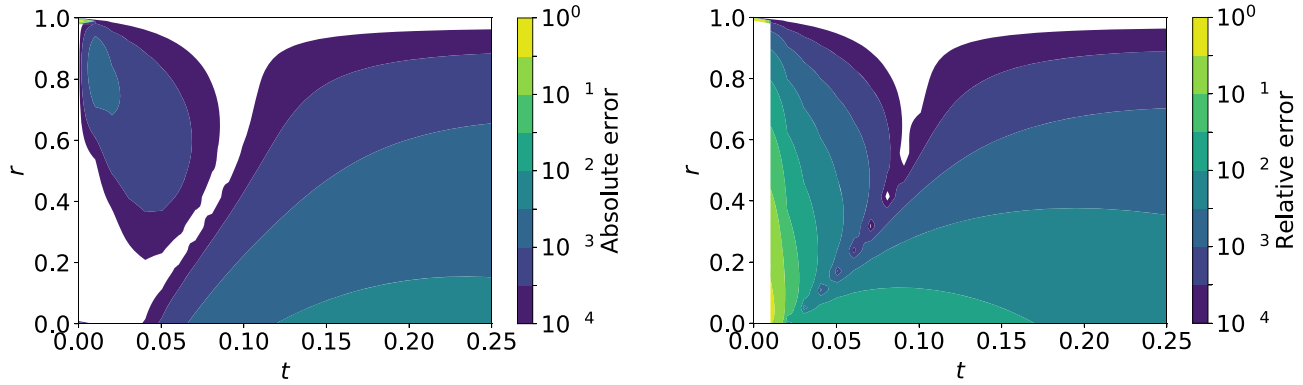

Figure 9. Comparison of the analytic and Crank–Nicholson scheme for diffusion into a cylinder with unity radius and unity diffusion coefficient. Left panel: absolute difference of the solutions. Right panel: relative difference of the solutions.

Using

$$\frac{\Delta t}{2} M^j = A\, \boldsymbol{n}^j \tag{A5}$$

the solution at time $t = t^{j+1}$ scheme can be written as

$$\boldsymbol{n}^{j+1} = (1 - A)^{-1}(1 + A)\boldsymbol{n}^j$$

where A is a tri-diagonal matrix with

$$A_{k,k} = -\alpha_k(\kappa'_{k-1/2} + \kappa'_{k+1/2}) \tag{A6}$$

$$A_{k,k+1} = \alpha_k\ \kappa'_{k+1/2} \tag{A7}$$

$$A_{k,k-1} = \alpha_k\ \kappa'_{k-1/2} \tag{A8}$$

with $\alpha_k = \Delta t/(2r_k\Delta r^2)$.

The boundaries are defined as $\left.\frac{\partial n}{\partial r}\right|_{r=0} = 0$ and $n(r_b, t) = Q(r, t)$. The outer boundary is solved simply by setting the outer point at r_b at each timestep. The inner, axial boundary is singular, so we solve the equation by defining the radial grid at half-integer steps (Hutchinson 2015), with $r_k = (k - 1/2)\Delta r$. Note that the first point $r_0 = -\Delta r/2$ is outside the solution grid and the matrix M starts with index $k = 1$. The first row of M is

$$M_1^j = \frac{1}{r_1\Delta r}\left[\kappa'_{1+1/2}\frac{n_{1+1}^j - n_1^j}{\Delta r} - \kappa'_{1-1/2}\frac{n_1^j - n_{1-1}^j}{\Delta r}\right].$$

The second term vanishes as $\kappa'_{1/2} = \kappa'(r = 0) = 0$. The remaining term is

$$M_1^j = \frac{1}{r_1\Delta r^2}\kappa'_{1+1/2}(n_2^j - n_1^j).$$

Consequently, the terms on the first row of A are

$$A_{1,1}^j = -\alpha_1\ \kappa'_{1+1/2} \tag{A9}$$

$$A_{1,2}^j = \alpha_1\ \kappa'_{1+1/2}. \tag{A10}$$

We show the solution to the diffusion equation Equation (A1), as solved with the Crank–Nicholson scheme in Figure 8, for $a = 1$ and constant $\kappa = 1$, with initially empty cylinder and a time-independent unity source at $r = 1$. To prevent numerical issues, we use slight smoothing of the initial $n(r,\ t = 0)$ at $r = 1$, using the smoothing function given by Equation (3).

The result shown in Figure 8 corresponds to diffusion into a cylinder with radius a and diffusion coefficient κ_0, when the radius, time, and diffusion coefficient are normalized with normalization constants r_n, t_n, and κ_n as

$$r = \hat{r}\ r_n,\ \text{ with }\ r_n = a \tag{A11}$$

$$t = \hat{t}\ t_n,\ \text{ with }\ t_n = \frac{a^2}{\kappa_0} \tag{A12}$$

$$\kappa = \hat{\kappa}\ \kappa_n,\ \text{ with }\ \kappa_n = \kappa_0. \tag{A13}$$

We use these normalization constants when comparing the diffusion equation solutions with particle simulations. It should be noted that in these units, the time particles diffuse a distance $s = a - r$ from the cylinder surface inwards, given as $\tau_d = s^2/(2\kappa)$, is

$$\hat{\tau}_d = 0.5\ (1 - \hat{r})^2 \tag{A14}$$

consistent with the parabolic shape of the $n(\hat{r},\ \hat{t}) = 1$ contour in Figure 8.

To verify the code, we compare it to the analytic solution of diffusion into an empty cylinder of radius a with constant diffusion coefficient κ (e.g., Dumbović et al. 2018),

$$n(r,\ t) = n_0\left(1 - \frac{2}{a}\sum_{n=1}^{\infty}\frac{J_0(\lambda_n r)}{\lambda_n\ J_1(\lambda_n a)}\mathrm{e}^{-\kappa\lambda_n^2 t}\right), \tag{A15}$$

where λ_n is defined by the positive roots of $J_0(\lambda_n a) = 0$. The comparison of the Crank–Nicholson scheme with the analytic result is shown in Figure 9. It should be noted that the analytic solution, Equation (A15), involves an infinite sum of oscillating Bessel functions, which converges very slowly. We used 1,000,000 terms in the sum, requiring 4 hr of computing time (for a single-node python script using scipy and numpy scientific libraries), resulting with initial density at cylinder axis of $n(r = 0,\ t = 0) = 0.0007\, n_0$ instead of the 0 given by the initial condition. Taking this into account, the Figure 9 demonstrates excellent agreement between the Crank–Nicholson scheme and the analytical result.

ORCID iDs

T. Laitinen https://orcid.org/0000-0002-7719-7783
S. Dalla https://orcid.org/0000-0002-7837-5780

References

Barnden, L. R. 1973, ICRC, 2, 1277
Benella, S., Grimani, C., Laurenza, M., & Consolini, G. 2019, NCimC, 42, 44

Burlaga, L., Sittler, E., Mariani, F., & Schwenn, R. 1981, JGR, 86, 6673
Cane, H. V. 2000, SSRv, 93, 55
Cane, H. V., Richardson, I. G., & Wibberenz, G. 1995, ICRC, 4, 377
Dalla, S., & Browning, P. K. 2005, A&A, 436, 1103
Dasso, S., Mandrini, C. H., Démoulin, P., & Luoni, M. L. 2006, A&A, 455, 349
Dumbović, M., Heber, B., Vršnak, B., Temmer, M., & Kirin, A. 2018, ApJ, 860, 71
Forbush, S. E. 1937, PhRv, 51, 1108
Fraschetti, F., & Jokipii, J. R. 2011, ApJ, 734, 83
Ghilea, M. C., Ruffolo, D., Chuychai, P., et al. 2011, ApJ, 741, 16
Gold, T., & Hoyle, F. 1960, MNRAS, 120, 89
Hutchinson, I. H. 2015, A Student's Guide to Numerical Methods (Cambridge: Cambridge Univ. Press)
Jokipii, J. R. 1966, ApJ, 146, 480
Krittinatham, W., & Ruffolo, D. 2009, ApJ, 704, 831
Kubo, Y., & Shimazu, H. 2010, ApJ, 720, 853
Laitinen, T., & Dalla, S. 2017, ApJ, 834, 127
Laitinen, T., Dalla, S., & Marriott, D. 2017, MNRAS, 470, 3149
Le Roux, J. A., & Potgieter, M. S. 1991, A&A, 243, 531
Leamon, R. J., Smith, C. W., & Ness, N. F. 1998, GeoRL, 25, 2505
Leske, R. A., Cohen, C. M. S., Mewaldt, R. A., et al. 2012, SoPh, 281, 301
Lockwood, J. A. 1971, SSRv, 12, 658
Luo, X., Potgieter, M. S., Zhang, M., & Feng, X. 2017, ApJ, 839, 53
Masías-Meza, J. J., Dasso, S., Démoulin, P., Rodriguez, L., & Janvier, M. 2016, A&A, 592, A118
Matthaeus, W. H., Qin, G., Bieber, J. W., & Zank, G. P. 2003, ApJL, 590, L53
Munakata, K., Yasue, S., Kato, C., et al. 2006, Advances in Geosciences, Vol. 2: Solar Terrestrial (ST) (Singapore: World Scientific), 115
Parker, E. N. 1965, P&SS, 13, 9
Quenby, J. J., Mulligan, T., Blake, J. B., Mazur, J. E., & Shaul, D. 2008, JGRA, 113, A10102
Richardson, I. G., & Cane, H. V. 2011, SoPh, 270, 609
Richardson, I. G., Cane, H. V., & Wibberenz, G. 1999, JGR, 104, 12549
Ruffolo, D., Pianpanit, T., Matthaeus, W. H., & Chuychai, P. 2012, ApJL, 747, L34
Ruffolo, D., Tooprakai, P., Rujiwarodom, M., et al. 2006, ApJ, 639, 1186
Sáiz, A., Ruffolo, D., Bieber, J. W., Evenson, P., & Pyle, R. 2008, ApJ, 672, 650
Shalchi, A. 2010, ApJL, 720, L127
Shalchi, A., Bieber, J. W., & Matthaeus, W. H. 2004, ApJ, 604, 675
Subramanian, P., Antia, H. M., Dugad, S. R., et al. 2009, A&A, 494, 1107
Thomas, S. R., Owens, M. J., Lockwood, M., & Scott, C. J. 2014, SoPh, 289, 2653
Torsti, J., Riihonen, E., & Kocharov, L. 2004, ApJL, 600, L83
Wibberenz, G., Le Roux, J. A., Potgieter, M. S., & Bieber, J. W. 1998, SSRv, 83, 309